applied sciences

MDPI

Article

Risk-Based Safety Assessment of Aging Lattice Steel Space-Truss Structures Under Extreme Winds: A Multi-Scale Wind and Multi-Degradation Coupling Framework with Application to Transmission Towers

Yu Wang [1], Dedong Yang [1], Hao Zhu [2], Jun Chen [2] and Daguang Han [3,*]

[1] State Grid Wenzhou Electric Power Supply Company, Wenzhou 325000, China
[2] School of Civil Engineering, Chongqing Jiaotong University, Chongqing 400074, China
[3] School of Civil Engineering, Southeast University, Nanjing 211189, China
* Correspondence: daguang.han@seu.edu.cn

Abstract

Extreme wind events, particularly tropical cyclones, pose the most severe safety threat to aging lattice steel space-truss structures in coastal regions, including transmission towers, communication and observation towers, and lattice supports of building-integrated wind-energy facilities. Such structures suffer progressive capacity degradation through multiple concurrent mechanisms, yet their actual residual safety margin under extreme wind loading remains poorly quantified. Current assessment practices rely on code-prescribed simplified wind speeds that ignore terrain-induced local amplification, and assume an intact structural condition that neglects in-service deterioration. This paper proposes a Risk-Based Safety Assessment Framework (RBSAF) that addresses both deficiencies through a five-step pipeline: (i) multi-scale wind field downscaling that resolves terrain-amplified wind profiles at individual structure sites; (ii) independent degradation models for atmospheric corrosion, bolt loosening, fatigue accumulation, and pitting corrosion; (iii) a multi-degradation coupling aggregation method that yields a unified Structural Health Index (SHI) capturing nonlinear interaction effects; (iv) code-based multi-scenario safety margin scanning with automatic identification of weak components; and (v) a risk-informed reinforcement priority mapping strategy. A representative 220 kV angle-steel lattice tower in a coastal mountainous corridor of Southeastern China is employed as the case study. Results show that after 30 years of service in an ISO 9223 C4 corrosive environment, the structure-level SHI decreases from 1.47 (intact, code wind) to 1.00 under the proposed coupled assessment with code-prescribed wind, and further to 0.76 when terrain amplification (15% speed-up) is considered, with the failure probability rising from 3.6% to 24.1%. Multi-degradation coupling causes an additional 28% capacity loss relative to single-factor assessment and substantially alters the weak-component ranking. Reinforcing the five most critical members restores the SHI to 1.25 with only a 2.8% steel-weight increase. The framework provides a systematic, quantitative tool for safety evaluation and maintenance prioritization of aging lattice steel structures in wind-prone built environments.

Academic Editor: Bostjan Brank

Received: 20 May 2026
Revised: 25 June 2026
Accepted: 1 July 2026
Published: 6 July 2026

Keywords: lattice steel structures; aging built environment infrastructure; extreme wind hazard; structural safety assessment; multi-degradation coupling; structural health index; risk-informed maintenance; complex terrain

1. Introduction

Aging lattice steel space-truss structures are a ubiquitous component of the modern built environment. They serve as load-bearing systems for tall communication and observation towers, long-span roof trusses in stadiums and exhibition halls, lattice supports of building-integrated and stand-alone wind-energy facilities, exposed industrial steel frames, and overhead transmission towers. Despite serving different functions, these structures share a common set of structural-engineering challenges: wind-induced dynamic loading on slender exposed members, stability of compression elements, integrity of bolted connections, and time-dependent material degradation over service lives that typically span 30–50 years. The progressive deterioration of such structures under combined environmental and mechanical actions has become an increasingly urgent concern for asset owners and building authorities worldwide, as a growing fraction of the installed stock approaches or exceeds its original design life. Transmission towers, the focus of the case study in this paper, represent one of the most heavily instrumented and well-documented members of this structural family, and are, therefore, an ideal benchmark for developing and validating safety assessment methodologies that are subsequently transferable to the broader built-environment context.

Overhead high-voltage transmission lines constitute the arterial network of modern power systems and are widely recognized as critical infrastructure whose failure can cascade into large-scale socioeconomic disruption [1,2]. Among all natural hazards, extreme wind events—tropical cyclones (typhoons/hurricanes), downbursts, and extratropical storms—are the dominant cause of structural failure in lattice transmission towers [3–5]. According to the CIGRÉ survey [6], wind-induced tower collapses account for more than 80% of weather-related transmission line failures globally. Recent decades have witnessed a rising frequency and intensity of tropical cyclones in the Western Pacific and North Atlantic basins, further exacerbating the vulnerability of coastal transmission corridors [7,8]. A single tower collapse can trigger cascading failure of adjacent towers through unbalanced conductor tension, with potential propagation across interdependent infrastructure systems [9,10], leading to prolonged outages and restoration costs that may exceed tens of millions of US dollars per event [11]. Ensuring the structural safety of transmission towers under extreme wind loading is therefore a matter of paramount engineering and societal importance.

Current design and assessment practices for transmission tower wind loading are governed by international standards such as IEC 60826 [1], EN 50341 [2], and ASCE Manual 74 [3], as well as various national codes. These standards specify basic wind speeds and exposure categories that are essentially regional statistical averages, applied uniformly to all towers within a given zone. While this approach is practical for design purposes, it fails to capture the pronounced local variations in wind speed caused by complex terrain features such as ridges, saddles, escarpments, and valley-channeling effects [4,12,13]. Field observations and numerical studies have demonstrated that terrain-induced speed-up ratios can reach 1.5–2.0 at isolated hilltops and ridge crests [14,15], meaning that actual wind speeds at certain tower sites may substantially exceed the code-prescribed values. Since aerodynamic wind load is proportional to the square of wind speed, even a 15% underestimation of wind speed translates into a 32% underestimation of wind load—a discrepancy that can shift a tower from "safe" to "critical" in terms of structural utilization [4,5]. Computational fluid dynamics (CFD) simulations can resolve terrain effects with high fidelity [14,15], but their computational cost (typically hours to days per site) renders them impractical for the batch-level assessment of hundreds of towers along a transmission corridor. Recent advances in physics-informed neural networks (PINNs) [16] and hybrid physics–data-driven approaches [17] offer promising avenues for efficient yet physically consistent wind field estimation, though their integration into a complete safety assessment workflow remains unexplored.

On the resistance side, current structural safety verification is performed under the assumption that the tower is in its as-designed, intact condition. In practice, however, lattice transmission towers are long-lived assets with typical service lives of 30–50 years, during which multiple degradation mechanisms operate concurrently [18–20]. Atmospheric corrosion is arguably the most pervasive threat: in coastal and industrial atmospheres classified as C3–C5 under ISO 9223 [21], cumulative section loss in angle-steel members can reach 10–20% over 20–30 years of exposure [22,23]. Bolted connections, which are the primary load-transfer mechanism in lattice towers, suffer progressive preload relaxation under sustained wind-induced vibrations, a phenomenon first systematically characterized by Junker [24] and subsequently studied extensively in fastener engineering [25,26]. Fatigue accumulation due to cyclic wind loading, although rarely leading to outright fracture within the design life, progressively consumes the fatigue endurance of stress-critical members according to the Palmgren–Miner cumulative damage rule [27,28]. Additionally, pitting corrosion creates localized stress concentrations that act as potential crack initiation sites, effectively reducing the member's load-carrying capacity beyond what uniform-section-loss models predict [29]. Each of these degradation mechanisms has been studied individually in the structural engineering literature; however, investigations that consider all four mechanisms simultaneously remain scarce.

More critically, these degradation mechanisms do not act independently. Corrosion reduces the net cross-sectional area, which in turn elevates the stress range under the same external load, thereby accelerating fatigue damage accumulation—a well-known synergistic effect in corroded steel structures [18,19]. Bolt loosening alters the internal load distribution within the tower, redirecting forces to members that may already have diminished capacity due to corrosion or pitting. The nonlinear interaction among multiple degradation modes means that the actual residual capacity of an aged tower is lower than what any single-factor or linearly superimposed multi-factor estimate would suggest. Despite its engineering significance, a systematic framework that couples these degradation mechanisms and quantifies their combined effect on the time-variant safety margin of lattice towers has not been established in the open literature.

From a risk management perspective, the absence of a unified framework that simultaneously addresses load-side precision (terrain-resolved wind) and resistance-side degradation coupling leaves a critical gap in the safety assessment chain [30,31]. Without a quantitative, time-variant measure of the safety margin, maintenance and reinforcement decisions are often based on prescriptive inspection schedules or engineering judgment rather than risk-informed prioritization. Structural reliability theory provides the mathematical apparatus for probability-based safety evaluation [30,32–36]; however, its application to lattice transmission towers with comprehensive multi-degradation modeling is still limited. Fragility analysis frameworks have been developed for transmission towers under wind loading [37,38], but typically assume intact structural conditions. Time-dependent fragility and reliability studies that incorporate progressive deterioration have been conducted for bridges and buildings [19,20], yet analogous work for transmission towers remains at a nascent stage.

To address these interrelated gaps, this paper proposes a Risk-Based Safety Assessment Framework (RBSAF) that integrates five sequential steps: (i) hazard characterization

https://doi.org/10.3390/app16136788

through multi-scale wind field downscaling, (ii) vulnerability modeling via four-category degradation assessment, (iii) multi-degradation coupling aggregation yielding a unified Structural Health Index (SHI), (iv) multi-scenario safety margin scanning with automatic weak-component identification, and (v) risk-informed reinforcement priority mapping. In contrast to prior studies that address a single degradation mechanism [18–20] or evaluate wind fragility under an as-designed, intact condition [37,38], and to terrain-wind studies that stop at the flow field without propagating it to a time-variant structural verdict [14,15], the present work is, to the authors' knowledge, the first to close the full loop—from terrain-resolved wind, through nonlinearly coupled four-mechanism degradation, to code-based safety checking and reinforcement decision-making—within a single self-consistent pipeline for aging lattice towers.

The main contributions of this paper are summarized as follows:

(1) A full-chain RBSAF framework is proposed that, to the best of the authors' knowledge, is among the first to integrate terrain-resolved wind loading, four-category degradation modeling, nonlinear degradation coupling, code-based safety checking, and reinforcement decision support into a single coherent pipeline for aging lattice transmission towers.

(2) Four independent degradation models—atmospheric corrosion, bolt loosening, fatigue accumulation, and pitting corrosion—are formulated and coupled through a physically motivated aggregation scheme to produce a unified, time-variant Structural Health Index (SHI) that accounts for cross-mechanism interaction effects.

(3) The combined impact of load-side refinement (terrain amplification) and resistance-side degradation coupling on the tower-level safety margin is systematically quantified via multi-scenario batch scanning across wind speed, wind direction, and service age, revealing failure probability evolution patterns that are invisible to conventional code-based assessment.

(4) A risk-informed reinforcement priority ranking method is developed that translates the assessment results into actionable maintenance decisions, demonstrating cost-effective interventions that restore the safety margin with minimal material addition.

The remainder of this paper is organized as follows. Section 2 presents the materials and methods, detailing the five-step RBSAF framework. Section 3 describes the case study configuration. Section 4 reports and discusses the results of the wind simulation, degradation assessment, coupling analysis, and risk quantification, together with their engineering implications, comparison with code-based practice, and limitations. Section 5 concludes with a summary of key findings and an outlook for future work.

2. Materials and Methods

2.1. Framework Overview

The proposed RBSAF comprises five sequential modules that collectively map the classical safety engineering paradigm of "hazard identification → vulnerability quantification → risk coupling → safety margin assessment → risk control" onto the specific problem of aging lattice transmission towers under extreme wind (Figure 1). The framework accepts four categories of input: (a) digital elevation model (DEM) terrain data, (b) meteorological observations or reanalysis fields providing inflow conditions, (c) structural design drawings or finite element models of the tower, and (d) service age and site-specific environmental parameters (corrosivity class, dominant wind direction, historical vibration statistics). The output is a tower-level risk map in which every member is color-coded according to a four-tier risk classification, accompanied by a ranked reinforcement priority list. Each of the five modules is described in Sections 2.2–2.6.

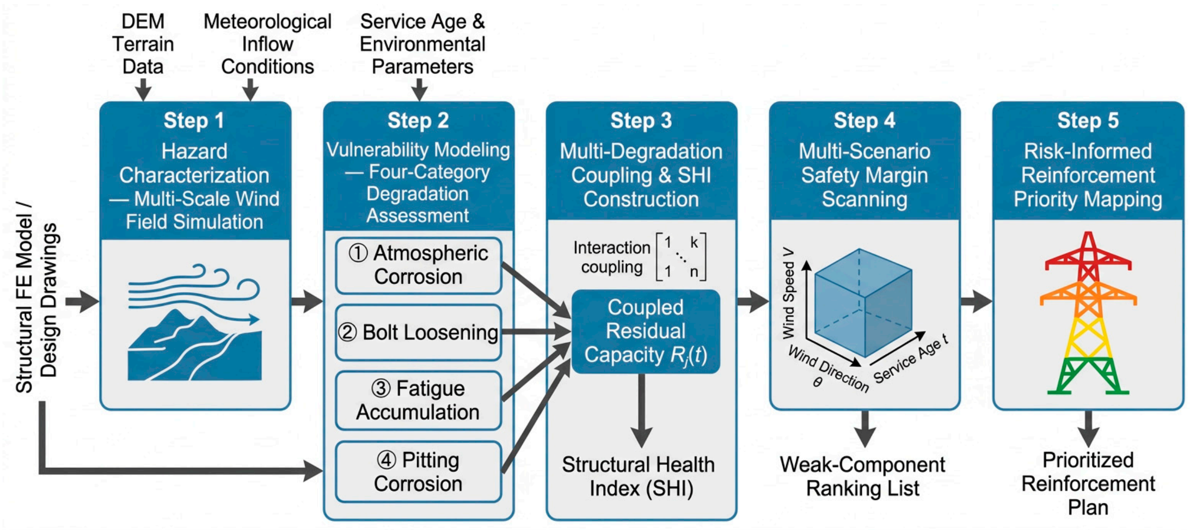

Figure 1. Schematic of the proposed five-step Risk-Based Safety Assessment Framework (RBSAF). Step 1: hazard characterization via multi-scale wind field simulation; Step 2: vulnerability modeling with four degradation categories; Step 3: multi-degradation coupling and Structural Health Index (SHI) construction; Step 4: multi-scenario safety margin scanning and weak-component identification; Step 5: risk-informed reinforcement priority mapping.

2.2. Step 1: Hazard Characterization via Multi-Scale Wind Field Simulation

Accurate characterization of the wind hazard at each tower site is the entry point of the assessment pipeline. The objective of this module is to downscale kilometer-resolution meteorological data (from reanalysis products or numerical weather prediction models) to meter-resolution wind profiles that resolve the local terrain effects on wind speed and turbulence [4,12,13]. Because aerodynamic wind load scales with the square of wind speed, modest improvements in wind-speed accuracy can significantly alter the safety assessment outcome. For instance, a 15% underestimation of the local wind speed due to neglected terrain amplification translates into a 32% underestimation of the design wind load, which can shift the stress ratio of a critical member from below to above the unity threshold.

The wind simulation module employed in this study is based on a three-dimensional mass-conservation wind field solver [14] that operates on a terrain-following coordinate system. The solver accepts the DEM of the region surrounding the tower site and the upstream boundary condition (reference wind speed at a specified height) and iteratively adjusts the three-dimensional velocity field until the continuity equation is satisfied throughout the computational domain. The solver enforces three-dimensional mass conservation $\nabla \cdot \mathbf{V} = 0$ on a terrain-following grid by adjusting an initial interpolated velocity field $\mathbf{V}_0$ through the variational minimization of $\int [\alpha_h^2((u-u_0)^2 + (v-v_0)^2) + \alpha_v^2(w-w_0)^2]dV$, subject to the continuity constraint, where α_h and α_v are the Gauss precision moduli controlling horizontal and vertical adjustment, respectively. The resulting Euler–Lagrange equation reduces to a Poisson equation for the Lagrange multiplier, solved by successive over-relaxation. It is acknowledged that this diagnostic mass-consistent approach does not resolve flow separation, recirculation, or turbulence dynamics that a prognostic RANS/LES solver would capture [14,15]; however, for the present objective—reconstructing steady-state mean wind profiles at heights of 10–50 m above ground at known tower locations on moderate-slope terrain—the trade-off between physical fidelity and computational cost (≈2 min per direction versus hours to days for CFD) is acceptable, and the simulated speed-up factor is cross-validated against empirical and analytical references in Section 4.1.

The solver outputs a steady-state velocity field at each grid node, from which the wind speed profile at the tower location is extracted and converted into member-level wind loads using the standard quasi-static approach specified in IEC 60826 [1] and EN 1991-1-4 [39]. The drag force on individual members is computed as:

$$F_w = 0.5 \cdot \rho \cdot C_d \cdot A \cdot V(z)^2 \quad (1)$$

where F_w (N) is the mean drag force on the member; ρ is the air density (1.225 kg/m³ at 15 °C and standard atmospheric pressure); C_d is the dimensionless drag (force) coefficient of the member cross-section, taken as 1.6 for sharp-edged angle-steel sections in the post-critical Reynolds-number regime per EN 1991-1-4 [39]; A (m²) is the member area projected onto the plane normal to the wind direction; and $V(z)$ (m/s) is the terrain-resolved 10-min mean wind speed at height z above ground. Gust effects are carried through the terrain-resolved gust speed used for $V(z)$, consistent with the quasi-static procedure of IEC 60826 [1]. Panel-level shielding and solidity effects are approximated here by applying the section drag coefficient to the net projected member area, a simplification relative to full solidity-ratio-based panel-drag formulations [4,39]; this assumption is listed among the limitations in Section 4.10. The wind direction is parametrically varied from 0° to 360° in 15° increments to capture directional effects [40]. For each direction, the complete wind load vector is assembled and applied to the structural model in the subsequent analysis steps.

It is important to emphasized that the RBSAF framework maintains an open interface for the wind module: other wind simulation tools (e.g., RANS-CFD, LES [15], or empirical topographic-multiplier methods [13]) can be substituted without altering the downstream assessment modules. The choice of wind solver affects the accuracy of hazard characterization but not the methodological structure of the framework.

2.3. Step 2: Vulnerability Modeling—Four-Category Degradation Assessment

The second module of the RBSAF quantifies the time-dependent capacity degradation of tower members through four mechanistic models. Unlike the single-point, intact-condition check prescribed by current design codes [41], this module explicitly accounts for the progressive loss of structural resistance over the service life. Each degradation mechanism is modeled independently in this section; their nonlinear interactions are addressed subsequently in Section 2.4.

2.3.1. Atmospheric Corrosion Degradation Model

Atmospheric corrosion is the most prevalent degradation mechanism for steel transmission towers, particularly in coastal, industrial, and tropical environments [21,22]. The rate and extent of corrosion depend on the atmosphere's corrosivity class, which is categorized from C1 (very low) to CX (extreme) under ISO 9223 [21]. In this study, the time-dependent corrosion depth is modeled using the widely adopted power-law function [18,22,23]:

$$d(t) = A \cdot t^{\,n} \quad (2)$$

where $d(t)$ is the cumulative corrosion depth (μm) at service age t (years), A is the first-year corrosion loss (μm), and n is the time exponent. The parameters A and n depend on the corrosivity class: for a C4 (high) environment typical of coastal regions, representative values are A = 80 μm and n = 0.59 [21,22]. For an equal-leg angle-steel member $L_b \times t_w$, assuming uniform corrosion on all exposed surfaces, the residual cross-sectional area at age t is:

$$A_r es(t) = 2 \cdot (b - 2d(t)) \cdot (t_w - 2d(t)) - (t_w - 2d(t))^2 \quad (3)$$

and the normalized section loss rate is defined as $\eta_{c(t)} = 1 - A_{res(t)}/A_0$, where A_0 is the original cross-sectional area. It is recognized that corrosion intensity varies with height along the tower: the splash zone near the base and the upper section exposed to wind-driven salt spray typically corrode faster than intermediate sections [22]. This height-dependent variation is incorporated by assigning adjustment factors (1.2 for the base zone, 1.0 for the body, and 1.1 for the cross-arm zone) to the parameter A.

2.3.2. Bolt Loosening Degradation Model

Bolted connections are the predominant joining method in lattice transmission towers, and their structural integrity depends critically on the clamping force provided by bolt preload. Under sustained dynamic loading, bolts experience progressive self-loosening through a mechanism first elucidated by Junker [24]: transverse cyclic slip at the thread and bearing interfaces causes incremental rotation of the nut, leading to a gradual decline in preload. This phenomenon has been confirmed by extensive experimental studies [25,26] and is particularly relevant for transmission towers, which are exposed to millions of wind-induced vibration cycles over their service life. The residual preload at service age t is modeled as an exponentially decaying function of cumulative vibration cycles:

$$F_p(t) = F_0 \cdot \exp(-\beta \cdot N(t)) \tag{4}$$

where F_0 is the initial preload at installation, β is the loosening rate coefficient (per cycle), and $N(t)$ is the cumulative number of significant vibration cycles up to age t. The parameter β depends on the bolt grade, surface finish, and prevailing vibration amplitude; typical values for Grade 8.8 M20 bolts (property class per ISO 898-1) under moderate wind-induced vibration lie in the range (0.5–2.0) × 10^{-7} per cycle [24,25]. The cumulative cycle count $N(t)$ is estimated by integrating the annual wind-speed probability distribution (typically Weibull-distributed) over the fundamental frequency of the tower structure [12]. Preload loss reduces the clamping friction on the gusset plate, leading to a decrease in the effective rotational stiffness of the connection node. This effect is represented by a connection stiffness retention factor $\kappa_b(t) = F_p(t)/F_0$, which is applied as a stiffness modifier to the corresponding degrees of freedom in the finite element model.

2.3.3. Fatigue Accumulation Model

Wind-induced cyclic loading subjects tower members to fluctuating stresses that, over decades of service, accumulate fatigue damage even if the peak stress amplitude remains well below the static yield strength. The fatigue life of steel members is characterized by the S–N curve (stress range versus number of cycles to failure), which for structural steels is specified in Eurocode 3 Part 1-9 [27] and related standards. In this study, the detail category-based S–N relationship is adopted:

$$N_f = C \cdot (\Delta\sigma)^{-\mathrm{m}} \tag{5}$$

where N_f is the number of cycles to failure at a constant stress range $\Delta\sigma$, and C and m are material constants determined by the detail category (for typical angle-steel members with bolted connections, m = 3 and C corresponds to a detail category of 71 MPa at 2 × 10^6 cycles [27]). Since wind loading produces a variable-amplitude stress history, cumulative fatigue damage is evaluated using the Palmgren–Miner linear damage accumulation rule [28]:

$$D_f = \Sigma(n_i/N_f, i) \tag{6}$$

where n_i is the number of cycles at stress range $\Delta\sigma_i$ extracted from the long-term wind-induced stress spectrum using the rainflow counting method, and N_f,i is the corresponding fatigue life from Equation (5). The fatigue damage index D_f ranges from 0 (undamaged) to 1 (fatigue failure). Although D_f approaching unity indicates imminent fatigue fracture, even intermediate values of D_f signify microstructural degradation (micro-crack initiation and growth) that erodes the member's reserve capacity. The static capacity reduction due to accumulated fatigue damage is approximated as a factor $(1 - k_f \cdot D_f)$ applied to the member's allowable stress, where k_f is an empirical coefficient in the range 0.3–0.5, reflecting the correlation between fatigue damage and residual fracture toughness [27,30]. The variable-amplitude stress history at each critical member is obtained by mapping the long-term wind-speed probability distribution (assumed Weibull-distributed with scale and shape parameters fitted from regional meteorological records) onto member axial stresses via the quasi-static drag relation in Equation (1) and the elastic finite element model. The annual cumulative cycle count is estimated as the product of the fundamental natural frequency of the tower ($f_1 = 2.4$ Hz for the case-study structure, obtained from modal analysis) and the fraction of time the wind exceeds the fatigue threshold (taken as 5 m/s), yielding the representative value $N(t)/t \approx 1.0 \times 10^5$ cycles per year .Rainflow counting is then applied to extract n_i at each stress range bin $\Delta\sigma_i$.

2.3.4. Pitting Corrosion Model

In addition to uniform atmospheric corrosion, localized pitting corrosion is prevalent on steel surfaces exposed to chloride-rich environments, particularly in coastal areas. Unlike general corrosion, which uniformly reduces the cross-section, pitting produces discrete hemispherical or conical cavities that act as stress concentration sites [29,42,43]. For structural carbon steels such as those examined here, pit nucleation in chloride-rich atmospheres is governed primarily by local breakdown of the surface film at second-phase microconstituents, with manganese-sulfide (MnS) inclusions identified as the most susceptible initiation sites [43,44]. The elastic stress concentration factor at a pit is approximated by the classical Inglis–Neuber solution:

$$K_t = 1 + 2\sqrt{\left(\frac{a}{\rho}\right)} \tag{7}$$

where a is the pit depth and ρ is the radius of curvature at the pit root. For a representative coastal C4 environment, pit depths of 1.0–2.5 mm after 20–30 years of service have been reported [21,29,42], yielding K_t values in the range of 2.0–4.5. The effect of pitting on the member's load-carrying capacity is modeled through an effective capacity retention factor:

$$\gamma_p(t) = 1 - (1 - 1/K_t(t)) \cdot \varphi \tag{8}$$

where φ is the fraction of the member surface affected by pitting (typically 3–8% for moderately pitted members [29]). This formulation acknowledges that pitting is localized: only the fraction φ of the member length experiences the elevated stress, while the remainder retains its full capacity. The overall effect is a modest but non-negligible reduction in the member's static strength that can be critical when superimposed on other degradation mechanisms.

2.4. Step 3: Multi-Degradation Coupling and Structural Health Index

The four degradation mechanisms described in Section 2.3 do not act in isolation. Their interaction produces synergistic effects that amplify the overall capacity loss beyond what independent superposition would predict. Three principal interaction pathways are identified and incorporated into the coupling model:

(a) Corrosion–fatigue interaction: As corrosion reduces the cross-sectional area by a fraction η_c, the stress range under the same external load increases:

$$\Delta\sigma_c orroded = \Delta F/[A_0 \cdot (1 - \eta_c)] \tag{9}$$

This elevated stress range enters Equation (5) and accelerates the fatigue damage accumulation. In the coupled model, the fatigue assessment is iteratively updated using the corroded cross-section, yielding a coupled fatigue damage $D_f^c(t)$ that is systematically higher than the uncoupled value $D_f(t)$ computed on the intact section. For the case study presented herein, coupling increases the 30-year fatigue damage from $D_f = 0.15$ (uncoupled) to $D_f^c = 0.22$ (coupled), representing a 47% amplification.

(b) Bolt loosening–stress redistribution: When connection stiffness decreases due to preload loss, the internal load distribution within the tower is altered. Members adjacent to loosened joints may attract a disproportionately higher share of the load, while others may be partially unloaded. This redistribution is captured by performing the finite element analysis with the degraded connection stiffness $\kappa_b(t)$ at each joint, producing a modified stress field $\sigma_j^b(t)$ that reflects the age-dependent load path.

(c) Pitting–general-corrosion superposition: At locations where pitting occurs on a member already thinned by general corrosion, the stress concentration $K_t(t)$ acts on a reduced-thickness substrate, amplifying the local peak stress beyond what either mechanism would produce alone.

These interactions are aggregated into a comprehensive, time-variant degradation function for each member j. The coupled residual capacity $R_{j(t)}$ is obtained by applying the degradation factors sequentially in a physically consistent order—first the section-level reduction (corrosion → reduced area → elevated stress), then the system-level redistribution (bolt loosening → modified load path), and finally the local amplification (pitting → stress concentration on the weakened section):

$$R_{j(t)} = \chi_j \cdot f_{\{y,j\}} \cdot A_{res}, j(t) \cdot \left[1 - k_f \cdot D^c_{\{f,j\}(t)}\right] \cdot \gamma_{\{p,j\}(t)} \cdot \frac{1}{1 + \delta_{\{b,j\}(t)}} \tag{10}$$

where χ_j is the buckling (stability) reduction factor of member j ($\chi_j = 1$ for tension- or yielding-governed members and $0 < \chi_j < 1$ for compression members, evaluated from the member slenderness per the column-buckling provisions of the applicable steel design code [41]); $f_{y,j}$ is the nominal yield strength (345 MPa for Q345 primary members, 235 MPa for Q235 secondary members); $A_{res,j}(t)$ is the corroded residual cross-sectional area from Equation (3); $D^c_{f,j}(t)$ is the corrosion-coupled fatigue-damage index from the iterative procedure of Equation (9); k_f is the fatigue–capacity coefficient (Table 1); $\gamma_{p,j}(t)$ is the pitting capacity-retention factor from Equation (8); and $\delta_{b,j}(t)$ is the dimensionless fractional stress increase caused by bolt-loosening-induced load redistribution at member j. The factor χ_j makes Equation (10) consistent with the stability check embedded in the allowable stress $f_{allow,j}(t)$ of Equation (12), ensuring that compression members are governed by buckling rather than yielding. Although $\delta_{b,j}(t)$ physically represents a load-side amplification, the term $1/(1 + \delta_{b,j}(t))$ is mathematically equivalent to an effective resistance-reduction factor; this keeps all degradation effects within the single capacity expression $R_j(t)$. The expression is dimensionally consistent because χ_j, $\left[1{-}k_f D^c_{f,j}\right]$, $\gamma_{p,j}$ and $1/(1 + \delta_{b,j})$ are all dimensionless while $f_{y,j} A_{res,j}$ carries units of force. The tower-level Structural Health Index is then defined as the minimum member-level safety ratio:

$$SHI_tower(t) = min_j R_j(t)/S_j \tag{11}$$

where S_j is the wind-load-induced force effect on member j. An SHI greater than 1.0 indicates that all members possess a positive safety margin under the given wind loading, whereas SHI ≤ 1.0 signifies that at least one member has reached or exceeded its degraded capacity. The SHI is a function of both service age (through R_j) and wind speed/direction (through S_j), enabling the construction of failure probability surfaces as described in Section 2.5. It is important to distinguish the SHI from conventional static utilization ratios: the latter are computed for intact structures under design loads, whereas the SHI explicitly incorporates the time-variant, coupled degradation state.

Table 1. Degradation model parameters, uncertainty ranges, and their sources.

Parameter	Symbol	Value	Uncertainty/Range	Source
First-year corrosion loss (depth)	A	80 μm	70–100 μm (±25%)	ISO 9223 C4 [21]
Corrosion time exponent	n	0.59	0.54–0.64 (±0.05)	[22]
Base-zone adjustment factor	—	1.2	1.1–1.3	[22]
Initial bolt preload (M20, Gr.8.8)	F_0	145 kN	±7%	[25]
Bolt loosening rate	β	1.0×10^{-7}/cycle	$(0.5–2.0) \times 10^{-7}$/cycle	[24]
Annual vibration cycles (est.)	—	1.0×10^5/yr	±50%	[12]
S–N slope exponent	m	3	detail-fixed	EC3-1-9 [27]
Detail category	—	71 MPa	±20% (scatter band)	EC3-1-9 [27]
Fatigue–capacity coefficient	k_f	0.4	0.3–0.5	[30]
Pitting pit depth at 30 yr	a	1.5 mm	1.0–2.5 mm	[21,29,42]
Pit root radius	ϱ	1.0 mm	±0.5 mm	[29]
Pitting surface fraction	φ	5%	3–8%	[21,29]

2.5. Step 4: Safety Margin Assessment via Multi-Scenario Scanning

The fourth module of the RBSAF evaluates the tower's safety margin across a comprehensive parameter space defined by wind speed, wind direction, and service age. The purpose is to answer the question: "Under what combination of conditions does the tower first become unsafe, and which member initiates failure?" This is the safety engineering equivalent of a systematic "what-if" analysis [31,33].

For each combination of wind speed V (ranging from 0.6 to 1.4 times the design wind speed, in increments of 0.1), wind direction θ (0–360°, in 15° increments), and service age t (0, 10, 20, 30 years), the following procedure is executed: (a) the wind load module (Section 2.2) generates the member-level force vector; (b) the finite element solver computes the stress distribution σ_j under the bolt-loosening-modified system stiffness; (c) each member's stress ratio SR_j is computed as:

$$SR_j = \sigma_j / f_a llow, j(t) \tag{12}$$

where $f_a llow$, $j(t)$ is the degradation-adjusted allowable stress, incorporating both strength checking (per the applicable steel design code [41]) and stability checking for compression members. Primary members (main legs, diagonals) and secondary members (horizontal bracings, redundant members) are distinguished by applying differentiated buckling reduction factors, consistent with international design practice for lattice towers [1–3,41].

A member with SR_j > 1.0 is deemed to have exhausted its structural capacity under the given scenario. The tower-level safety index for a given scenario is $SHI(V,\theta,t) = min_j 1/SR_j$, consistent with Equation (11). By aggregating the results across all scenarios, the following outputs are generated: (a) the critical wind speed at which the first member reaches SR = 1.0, for each age; (b) the failure probability surface $P_f(V,t)$, obtained by assuming a wind-speed distribution and integrating the fragility curve [35,38]; (c) a ranked list of the N most vulnerable members at each age, including their locations, failure modes (yielding vs. buckling), and SR values.

The failure probability in (b) is computed through an explicit reliability formulation that separates the wind hazard, the structural fragility, and their convolution.

Wind hazard model. Because tower failure is governed by the annual extreme wind, the annual-maximum 10-min mean wind speed is described by a Gumbel (Type I extreme-value) distribution:

$$F_{V(v)} = \exp\left\{-\exp\left[-\frac{v-u}{\alpha}\right]\right\} \tag{13}$$

whose location u and scale α are fitted from the regional return-period values (V_{50} = 35.0 m/s, V_{100} = 38.5 m/s; Section 3.2), giving u ≈ 15.4 m/s and α ≈ 5.0 m/s, with $V_T = u - \alpha \cdot \ln\left[-\ln\left(1 - \frac{1}{T}\right)\right]$. This extreme-value model is deliberately tail-weighted so that rare, high-intensity events—the dominant contributors to failure—are represented correctly, whereas the Weibull parent distribution used for fatigue cycle counting (Section 2.3.3) would underestimate the upper tail.

Structural fragility. For each service age t, the conditional failure probability given a wind speed V is represented by a lognormal cumulative distribution function:

$$P_{f(V|t)} = \Phi\left[\frac{\ln\left(\frac{V}{m_{R(t)}}\right)}{\beta_R}\right] \tag{14}$$

where $\Phi(\cdot)$ is the standard normal CDF, $m_{R(t)}$ is the median wind-speed capacity (the speed at which the tower-level SHI = 1.0 at age t), and β_R is the logarithmic standard deviation. Both parameters are estimated directly from the multi-scenario scanning: at each age the SHI = 1.0 crossing is located for every wind direction and every Latin-hypercube parameter draw, and $m_{R(t)}, \beta_R$ are taken as the median and logarithmic standard deviation of the resulting capacity sample [38].

Failure probability (hazard–fragility convolution). The annual failure probability at age t is obtained by convolving the fragility with the hazard:

$$P_{f(t)} = \int_0^{\infty} P_{f(V|t)} \cdot f_{V(v)dv} \tag{15}$$

where $f_{V(v)} = \frac{dF_V}{dv}$ is the Gumbel density. Equation (15) is evaluated by direct numerical (trapezoidal) integration over a fine wind-speed grid. Once the fragility is established, the reliability problem is effectively one-dimensional in wind intensity; this direct integration is therefore exact to quadrature precision and is preferred over first-/second-order reliability methods (FORM/SORM), which would introduce limit-state linearization error. The two reported hazard scenarios—code wind and terrain-amplified wind—correspond to the same fragility convolved with hazard distributions whose characteristic speed differs by the terrain speed-up factor (1.15).

Two-level treatment of uncertainty. The convolution in Equation (15) propagates the aleatory (year-to-year) variability of the wind. The epistemic uncertainty in the degradation parameters (Table 1) is propagated at a second, outer level by the 1000-sample Latin-hypercube Monte-Carlo procedure of Section 4: each realization regenerates $m_{R(t)}, \beta_R$ and hence a value of $P_{f(t)}$, and the 5th–95th percentiles of the ensemble constitute the confidence bands reported in Section 4, with the quoted point estimates being the ensemble medians.

Significance of degradation mechanisms. A variance-based global sensitivity analysis is performed on the same Latin-hypercube sample. The first-order Sobol index of mechanism *i* is

$$S_i = \frac{Var[E(Y|X_i)]}{Var(Y)} \tag{16}$$

where Y is the critical-member capacity loss (equivalently the structure-level SHI) and X_i denotes the parameter group of mechanism *i* (atmospheric corrosion, fatigue, bolt loosening, or pitting). The interaction share $1 - \Sigma_i S_i$ measures the fraction of output variance attributable to inter-mechanism coupling, giving an explicit, reproducible ranking of degradation significance.

https://doi.org/10.3390/app16136788

2.6. Step 5: Risk-Informed Reinforcement Priority Mapping

The final module translates the quantitative safety assessment into actionable maintenance recommendations by constructing a four-tier risk classification and a reinforcement priority ranking.

Four risk levels are defined based on the member stress ratio under the design wind speed at the assessed service age: Level I (Safe): SR < 0.70, indicating ample reserve—routine maintenance suffices; Level II (Attention): 0.70 ≤ SR < 0.85, suggesting reduced but adequate reserve—enhanced inspection is recommended; Level III (Warning): 0.85 ≤ SR < 1.00, signaling a thin margin—reinforcement planning should be initiated; Level IV (Critical): SR ≥ 1.00, indicating capacity exceedance—immediate intervention is required.

Consistent with the classical definition of risk as the product of likelihood and consequence [30,31], the reinforcement priority of each member is quantified by an explicit member-level risk score:

$$Risk_{j(t)} = P_{\{f,j\}(t)} \cdot \left[w_I \cdot I_j + w_C \cdot C_j \right] \tag{17}$$

where $P_{\{f,j\}(t)}$ is the member-level failure probability obtained from the member fragility (Equations (14) and (15)) at the assessed age; $I_j \in (0, 1]$ is the normalized structural-importance weight (primary leg members → $I_j \approx 1.0$, redundant bracings → $I_j \approx 0.2$); $C_j \in (0, 1]$ is the consequence-severity weight, set higher when loss of the member triggers progressive collapse of adjacent members [10,45,46]; and w_I, w_C are expert-assigned weights ($w_I + w_C = 1$; $here\ w_I = 0.6, w_C = 0.4$). The four-tier SR classification serves as a rapid deterministic screen that flags Level III and IV members, whereas Equation (17) supplies the probabilistic risk ranking that orders those flagged members for reinforcement; together they constitute the risk-based decision layer of the framework. A weighted scoring formula is used to rank all Level III and IV members, producing a prioritized reinforcement list. For the top-ranked members, candidate reinforcement measures (section enlargement, member replacement, or addition of supplementary bracing) are evaluated by updating the finite element model with the reinforced member properties and re-running the safety assessment. The resulting SHI improvement per unit of added steel mass provides a cost-effectiveness metric that guides resource allocation.

3. Case Study

3.1. Tower Description

The proposed framework is demonstrated on a representative 220 kV single-circuit angle-steel lattice transmission tower located in a coastal mountainous corridor of Southeastern China. The tower has a total height of 42 m, a base width of 8.2 m, and a nominal height (from base to conductor attachment) of 33 m (geometric dimensions carry the GB/T 2694 fabrication tolerances for hot-rolled angles: ±1.5% on leg width and ±0.6 mm on thickness for t ≤ 16 mm). The structural system comprises 186 nodes and 523 angle-steel members, including 148 primary members (main legs, body diagonals, and cross-arm chords) and 375 secondary members (horizontal bracings, sub-diagonals, and redundant members). The primary members are fabricated from Q345 steel (nominal yield strength 345 MPa) and the secondary members from Q235 steel (nominal yield strength 235 MPa). Both are hot-rolled structural carbon steels with a ferritic–pearlitic microstructure; no martensitic phase is present in the as-delivered, unwelded, bolt-assembled angle profiles. Their nominal chemical compositions (wt.%) are, for Q235 (GB/T 700): C ≤ 0.22, Mn ≤ 1.40, Si ≤ 0.35, P ≤ 0.045, S ≤ 0.050; and for Q345/Q355 (GB/T 1591): C ≤ 0.20, Mn ≤ 1.70, Si ≤ 0.55, P ≤ 0.035, S ≤ 0.035, with trace Nb/V/Ti micro-alloying. At the microstructural scale, pitting is preferentially initiated at MnS inclusions and along pearlite/ferrite segregation bands, which form local micro-galvanic couples with the surrounding matrix and act as pit-initiation sites [29,43,44]. In service the members are hot-dip galvanized; the bare-steel corrosion parameters adopted in Section 2.3.1, therefore, represent the conservative post-zinc-depletion stage, and the protective effect of the zinc layer is discussed as a limitation in Section 4.10.

The principal member sections are listed in Table 2. The design basic wind speed at 10 m height (50-year return period) is 35 m/s per the applicable loading code [1,39], with an estimated ±8% epistemic uncertainty arising from the extreme-value fit to the regional wind record. The foundation type is a reinforced-concrete stepped footing, assumed rigid in the structural model.

Table 2. Principal member sections of the case-study tower.

Member Group	Section	Steel Grade	Count
Main leg (lower)	L160 × 12	Q345	16
Main leg (upper)	L140 × 10	Q345	12
Body diagonal	L125 × 8	Q345	48
Cross-arm chord	L100 × 7	Q345	32
Horizontal bracing	L75 × 5	Q235	64
Sub-diagonal	L63 × 5	Q235	120
Redundant	L50 × 4	Q235	231

3.2. Extreme Wind Scenario Design

Four representative extreme wind scenarios are designed based on the regional wind climate statistics and historical return-period analysis:

Scenario A: 50-year return period wind (V_{10} = 35.0 m/s), representing the code-prescribed design basis. Scenario B: 100-year return period wind (V_{10} = 38.5 m/s), representing a moderately exceeding event. Scenario C: Design wind speed amplified by terrain effects (V_{10} = 40.3 m/s, corresponding to a terrain speed-up factor of 1.15), representing the actual condition at a tower site on a pronounced ridge. Scenario D: The most unfavorable wind direction identified by preliminary directional analysis (θ = 45° from the longitudinal axis) at the Scenario A wind speed, targeting the weakest directional capacity surface [40]. The return-period wind speeds carry an estimated ±8% uncertainty band (extreme-value sampling error) and the terrain speed-up factor an estimated ±15% band (cross-validated in Section 4.1); these bands are propagated to all derived results in Section 4. For each scenario, a full 360° directional sweep in 15° increments is also performed for the multi-scenario scanning in Section 2.5.

3.3. Computational Setup

The wind simulation domain covers a 5 km × 5 km area centered on the tower site with a horizontal grid resolution of 10 m and 40 vertical layers up to 500 m above ground. The DEM is derived from freely available SRTM 30 m elevation data, resampled to match the computational grid. The upstream boundary condition is the reference wind speed at 10 m height corresponding to each scenario.

The structural finite element model is a three-dimensional truss model in which each member is represented by a two-node bar element (axial force only). Gusset plate eccentricities are accounted for through effective-length adjustments. The structural solver is implemented in Python with a direct sparse-matrix solution strategy, capable of solving the full system in less than 0.5 s per load case. The degradation model parameters are summarized in Table 2. The corrosivity class is C4 (coastal, high salinity) per ISO 9223 [21]. Four service ages are analyzed: 0 years (intact baseline), 10, 20, and 30 years. To support reproducibility and repeatability, the full workflow is specified as follows. The wind and structural solvers are implemented in Python 3.11 (Python Software Foundation, Wilmington, DE, USA) with NumPy 1.24 and SciPy 1.10 (sparse direct solver scipy.sparse.linalg.spsolve). The mass-consistent wind field is converged by successive over-relaxation (relaxation factor 1.8) to a normalized residual tolerance of 1×10^{-6}. A grid-independence study at 20 m, 10 m, and 5 m horizontal resolution showed less than 1.5% variation in the ridge-top speed-up factor between the 10 m and 5 m grids, confirming convergence at the adopted 10 m resolution. All computations are deterministic for fixed inputs, except the Monte-Carlo uncertainty propagation (Section 4), for which the random seed is fixed (seed = 42) to guarantee repeatability. The source scripts, DEM identifiers and parameter files are available from the corresponding author on request and will be deposited in a public repository upon acceptance.

4. Results and Discussion

Unless otherwise stated, quantitative results below are reported with an uncertainty band obtained by propagating the parameter ranges of Table 1 and the wind-speed/terrain bands of Section 3.2 through the assessment pipeline, using one-at-a-time perturbation supplemented by a 1000-sample Latin-hypercube Monte-Carlo run (seed = 42); the band denotes the 5th–95th percentile interval. Because the degradation parameters are taken from the literature rather than from site-specific inspection, these bands quantify epistemic rather than purely aleatory uncertainty and should be read as indicative confidence ranges.

4.1. Wind Field Simulation Results

Figure 2 presents the simulated wind field over the study area at a reference inflow speed of 35 m/s from the east. The terrain in the study area features coastal hills with elevations ranging from 20 m to 380 m above sea level and maximum slope gradients exceeding 35°. The wind field exhibits pronounced terrain-induced features: (a) speed-up zones on exposed ridges and hilltops where the local wind speed reaches 40–43 m/s (14–23% above the reference), (b) deceleration zones in the lee of ridges where the wind speed drops to 25–30 m/s, and (c) channeling effects in narrow valleys that locally amplify speeds by 10–15%. These heterogeneities are entirely absent from the uniform code-prescribed wind speed, which would assign 35 m/s everywhere.

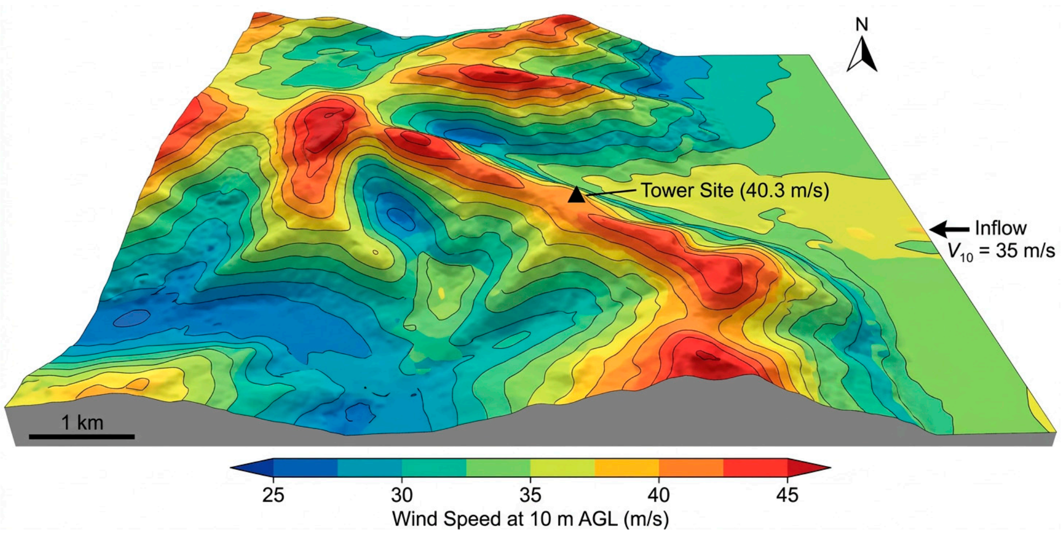

Figure 2. Three-dimensional wind speed contour map over the study area (inflow V_{10} = 35 m/s, from east). Colors indicate local wind speed at 10 m above ground: blue (<30 m/s), green (30–35 m/s), yellow (35–40 m/s), red (>40 m/s). Black triangle marks the case-study tower site.

At the case-study tower site, which is positioned on a moderate ridge (elevation 210 m, local slope 22°), the simulated wind speed at 10 m is 40.3 m/s—a terrain speed-up factor of 1.15 relative to the reference value of 35 m/s. Figure 3 compares the simulated vertical wind profile at the tower site with the code-prescribed logarithmic profile. The code profile underestimates the wind speed at all heights, with the discrepancy peaking at approximately 20 m above ground (the elevation of the lower body section) where it reaches 18%. At the conductor attachment height (33 m), the discrepancy is 12%. Table 3 summarizes the wind speed comparison at key heights.

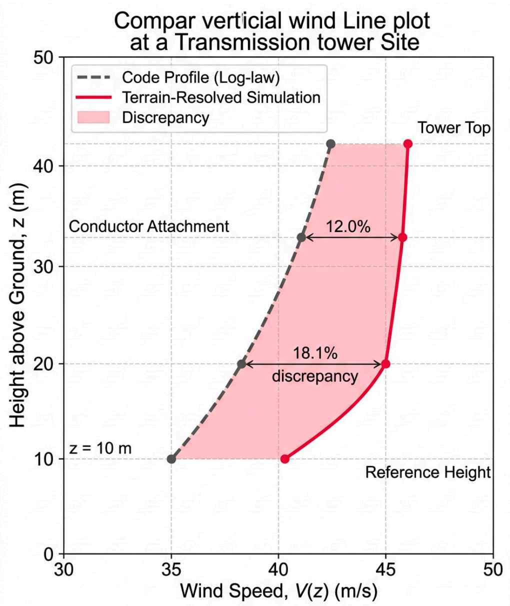

Figure 3. Comparison of vertical wind speed profiles at the tower site: terrain-resolved simulation (solid line) versus code-prescribed profile (dashed line). The shaded area represents the discrepancy band.

Table 3. Wind speed comparison between code profile and terrain-resolved simulation at the tower site.

Height (m)	Code V (m/s)	Simulated V (m/s)	Discrepancy (%)
10	35.0	40.3	+15.1
20	38.2	45.1	+18.1
33	40.8	45.7	+12.0
42 (tower top)	42.1	46.2	+9.7

To corroborate the credibility of the simulated wind field, the speed-up factor of 1.15 obtained at the ridge tower site is cross-checked against two independent sources: (i) the empirical topographic-multiplier formula in EN 1991-1-4 Annex A.3 [39], which for a ridge of upwind slope 0.40 (≈22°) and the tower located within 0.1·L_e of the crest yields a multiplier of $c_o \approx 1.18$ at 10 m height; and (ii) the analytical solution of Jackson and Hunt [13] for low-hill flow, which predicts a fractional speed-up Δs/U ≈ 2·H/L ≈ 0.16 for the local geometry. The simulated value (0.15) lies between the two reference values (0.16 and 0.18) and within their commonly accepted ±15% uncertainty band, providing reasonable independent verification of the wind-field result at the assessment-relevant location. It should be emphasized that this verification applies to the windward face and crest of the ridge, where the flow remains attached for the 22° slope considered—appreciable separation on such terrain is largely confined to the lee side and to slopes steeper than roughly 25–30° [14,15]. Because the case-study tower stands at the crest, the assessment-relevant speed-up is governed by attached, accelerating flow that the mass-consistent solver reproduces acceptably. Three caveats nonetheless apply. (i) The simulated speed-up (0.15) sits marginally below both independent references (0.16 and 0.18), indicating a slight tendency of the diagnostic solver to under-predict the crest acceleration; this small non-conservative bias lies within the ±15% band propagated to all results, but the upper-bound multiplier could be adopted for design-critical screening. (ii) For wind directions oblique to the crest the effective upwind slope, and hence, the speed-up, decreases, so the crest-perpendicular case used as the governing scenario is the conservative bound on speed-up magnitude; a tower sited on the lee side, by contrast, would lie in a separated wake that only a prognostic RANS/LES model could resolve. (iii) As a steady mean-flow solver the model does not generate turbulence statistics, and the resulting under-representation of turbulence is carried by the gust-based loading (Section 2.2) and quantified as a dynamic-amplification limitation in Section 4.10.

4.2. Degradation Assessment Results

Figure 4 presents the evolution of the four degradation indicators over the 30-year service life. Panel (a) shows the atmospheric corrosion section loss rate $\eta_c(t)$ for representative members. For the main leg member L160 × 12 at the base zone (with the 1.2× adjustment factor), η_c reaches 8.2% at 10 years, 14.3% at 20 years, and 19.6% at 30 years. For the cross-arm chord L100 × 7, the corresponding values are 5.4%, 9.5%, and 13.1%. The nonlinear (decelerating) growth pattern reflects the time exponent n = 0.59 < 1, consistent with the formation of partially protective corrosion products that slow the diffusion of corrosive species.

Panel (b) illustrates the bolt preload retention factor $\kappa_b(t)$. Under the assumed cumulative vibration exposure of 1 × 10^5 cycles per year, the preload declines to $\kappa_b = 0.90$ at 10 years, 0.82 at 20 years, and 0.74 at 30 years, representing a 26% loss of clamping force after three decades of service. Panel (c) presents the fatigue damage index $D_f(t)$ for the most fatigue-critical member (a diagonal brace in the waist section subjected to the highest stress range). Under the uncoupled assumption, D_f reaches 0.06 at 10 years, 0.10 at 20 years, and 0.15 at 30 years. Panel (d) shows the pitting capacity retention factor $\gamma_p(t)$: starting from 1.00 (no pitting), it decreases to 0.95 at 10 years, 0.88 at 20 years, and 0.82 at 30 years as pits deepen.

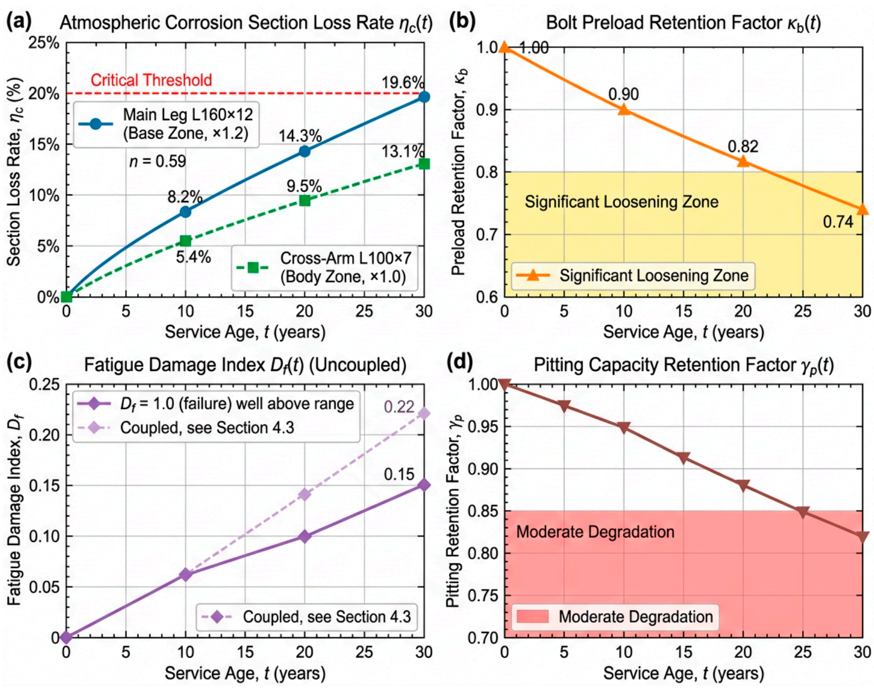

Figure 4. Evolution of degradation indicators over 30 years: (**a**) atmospheric corrosion section loss rate $\eta_c(t)$ for representative members; (**b**) bolt preload retention factor $\kappa_b(t)$; (**c**) fatigue damage index $D_f(t)$, uncoupled; (**d**) pitting capacity retention factor $\gamma_p(t)$. Shaded bands denote the 5th–95th percentile range obtained by propagating the parameter uncertainties of Table 2. Note: these curves are model predictions calibrated to literature values for the ISO 9223 C4 class, not site-specific measurements; they should be validated against in-situ ultrasonic thickness, bolt-torque, and metallographic pit-depth surveys before tower-specific deployment.

4.3. Multi-Degradation Coupling Effects

Figure 5 presents a coupling-effect matrix quantifying the interaction strength between each pair of degradation mechanisms at 30 years of service. The matrix is populated by computing the additional capacity reduction attributable to each interaction pathway beyond what independent superposition predicts. Three key observations emerge:

First, the corrosion–fatigue interaction is the strongest coupling effect: corrosion-induced section loss elevates the stress range by $1/(1-\eta_c)$, which enters the S–N curve with a cubic exponent (m = 3), producing a disproportionate acceleration of fatigue damage. At 30 years, the coupled fatigue damage index D_f^c = 0.22 exceeds the uncoupled value D_f = 0.15 by 47%. Second, the bolt-loosening effect on stress redistribution produces a 5–7% stress increase on members adjacent to heavily loosened joints, particularly in the hip section where connection density is high. Third, the superposition of pitting on a generally corroded substrate amplifies the effective stress concentration beyond what pitting on intact material would produce, but this effect is relatively modest (2–3% additional capacity loss) due to the small pitting surface fraction (5%).

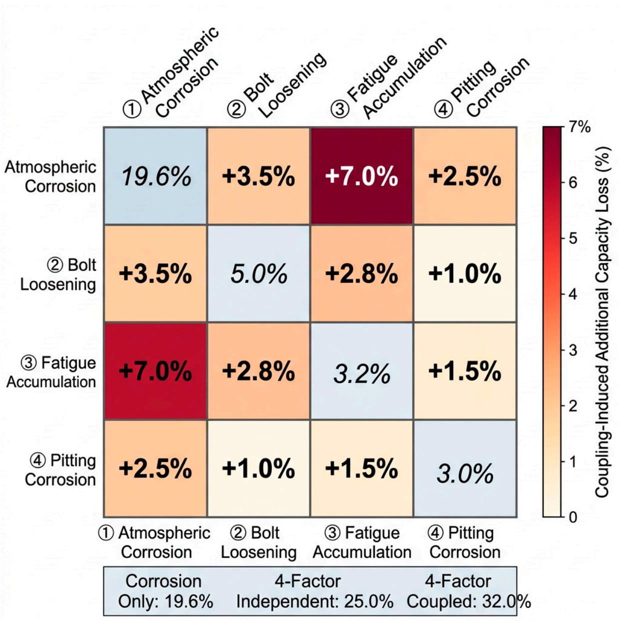

Figure 5. Multi-degradation coupling effect matrix at 30 years of service. Cell values represent the additional capacity reduction (%) attributable to each interaction pathway beyond independent superposition. Darker color indicates stronger coupling.

To quantify the overall impact of coupling, three assessment strategies are compared for the most critically loaded member (a main leg in the base zone) at 30 years: (a) single-factor assessment considering corrosion only: capacity loss = 19.6%, residual capacity ratio = 0.80; (b) four-factor independent superposition (no interaction): capacity loss = 25.0%, residual capacity ratio = 0.75; (c) four-factor coupled aggregation (proposed method): capacity loss = 32.0%, residual capacity ratio = 0.68. The coupled assessment reveals a 28%

greater capacity loss than the single-factor approach and a 9.3% greater loss than independent superposition, demonstrating that neglecting coupling leads to a systematic overestimation of the safety margin. The variance-based significance analysis (Equation (16)) ranks the four mechanisms quantitatively. The first-order Sobol indices of the structure-level SHI are $S_{corrosion} \approx 0.45$, $S_{fatigue} \approx 0.20, S_{bolt} \approx 0.13$, and $S_{pitting} \approx 0.06$, identifying atmospheric corrosion as the single most influential factor and pitting as the least. The interaction share, $1 - \Sigma S_i \approx 0.16$, confirms that roughly one-sixth of the variance in the residual safety margin arises from inter-mechanism coupling rather than from any factor acting alone—a quantitative corroboration of the coupling matrix in Figure 5 and of the corrosion–fatigue synergy in particular.

4.4. Safety Margin and Weak-Component Identification

Figure 6 displays full-tower stress ratio (SR) color maps for the intact tower (0 years) and the 30-year aged tower under Scenario A (code-prescribed wind V_{10} = 35 m/s, most unfavorable direction). In the intact condition, the maximum SR is 0.68, occurring at a main leg member in the lower body; all members remain comfortably below 1.0, and the tower-level SHI is 1.47 (5th–95th percentile: 1.41–1.53). After 30 years of coupled degradation, the stress pattern changes markedly: the maximum SR rises to 1.00, indicating that the most critical member has just reached its degraded capacity. The tower-level SHI is accordingly 1.00 (5th–95th percentile: 0.88–1.13), signifying that the tower is operating at the boundary of structural safety under the very wind speed it was designed to withstand.

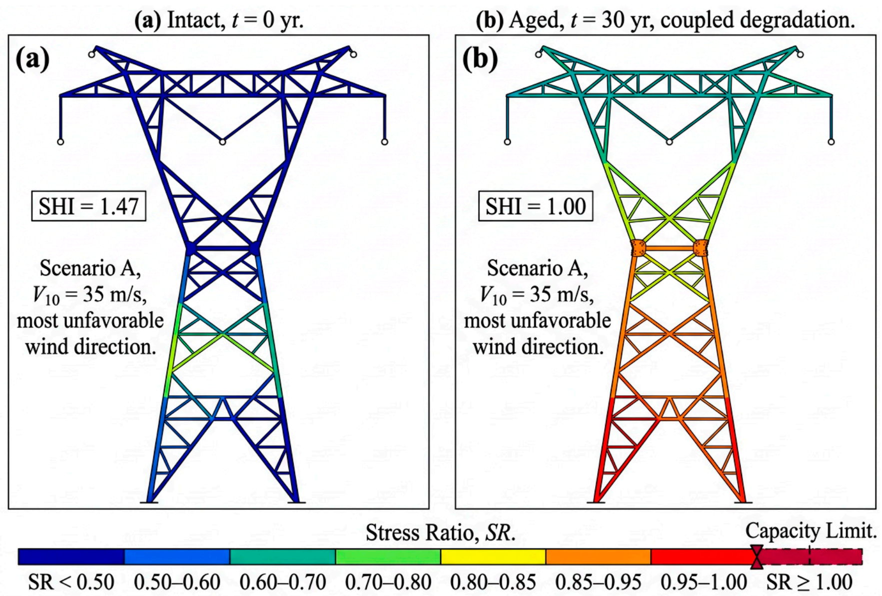

Figure 6. Full-tower stress ratio (SR) color maps: (**a**) intact tower (0 years); (**b**) 30-year aged tower with coupled degradation. All under Scenario A (V_{10} = 35 m/s). Color scale: blue (SR < 0.5), green (0.5–0.7), yellow (0.7–0.85), orange (0.85–1.0), red (SR ≥ 1.0).

Figure 7 compares the top-10 weakest members identified under the three assessment strategies at 30 years. Under single-factor (corrosion-only) assessment, the top-ranked members are concentrated in the lower body zone where corrosion is most severe. Under four-factor independent assessment, the ranking shifts slightly as fatigue and bolt effects elevate the risk at the waist section. However, under the proposed coupled assessment, a substantial reordering occurs: two members at bolted connection zones in the hip section (Members M-14 and M-21) that ranked 6th and 8th in the independent assessment rise to 2nd and 4th place, reflecting the amplified effect of bolt loosening combined with corrosion-accelerated fatigue. This finding is particularly significant for maintenance practice, as it implies that an operator relying on single-factor corrosion inspection would overlook these connection-zone vulnerabilities entirely.

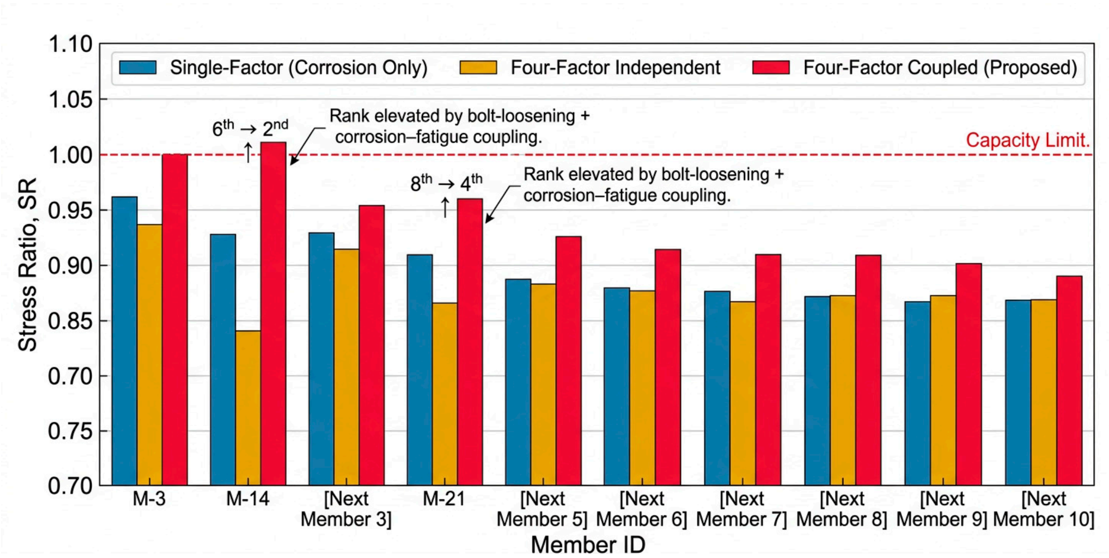

Figure 7. Top-10 weakest-member ranking under three assessment strategies at 30 years of service. Members are identified by a generic code (M-1 through M-523). Bar height represents the stress ratio SR. Different bar colors denote: single-factor (corrosion only), four-factor independent, and four-factor coupled (proposed).

The evolution of the tower-level SHI across service ages and wind scenarios is summarized as follows. Under Scenario A (code wind, no terrain amplification): SHI = 1.47 (0 yr), 1.31 (10 yr), 1.09 (20 yr), 1.00 (30 yr). The tower remains nominally safe throughout its service life when assessed against the code-prescribed wind, though the margin has been entirely depleted by 30 years. Under Scenario C (terrain-amplified wind, speed-up factor 1.15): SHI = 1.11 (0 yr), 0.99 (10 yr), 0.83 (20 yr), 0.76 (30 yr); the 30-year value carries a 5th–95th percentile band of 0.66–0.87. With terrain effects included, the tower becomes structurally insufficient as early as the 10th year of service—a finding that is invisible to conventional code-based assessment. The sensitivity of this timeline to the degradation parameters was examined by re-running the assessment at the upper-bound parameter set (Table 2: A = 100 μm, β = 2.0 × 10^{-7}/cycle, pit depth = 2.5 mm). Under code wind, the age at which the structure-level SHI first reaches 1.0 advances from 30 years (median parameters) to approximately 22 years; under terrain-amplified wind, the SHI falls below 1.0 before the 10th year rather than at it. Adverse-but-plausible parameter values can thus bring a "critical" classification forward by roughly 8–10 years, confirming the reviewer's concern and underscoring that the deterministic point estimates must be read together with the 5th–95th percentile bands reported throughout Section 4 and with the Sobol ranking of Section 4.3, which identifies atmospheric corrosion—followed by fatigue—as the parameters most worth constraining through inspection.

4.5. Risk Quantification and Decision Support

Figure 8 presents the failure probability map P_f as a function of wind speed ratio (V/V_design) and service age, obtained by integrating the fragility function (a lognormal cumulative distribution function fitted through the multi-scenario scanning results [38]) over the wind-speed distribution. At zero service age, the failure probability under the design wind speed is extremely low (P_f = 0.08%), as expected for a properly designed structure. This probability increases monotonically with both wind speed and age. At 30 years under code wind, P_f reaches 3.6% (2.1–6.0%); when terrain amplification is included, it rises to 24.1% (17–33%), indicating that the tower has degraded into a high-risk asset that requires urgent intervention. Plotting the independent-superposition and coupled surfaces together (Figure 8) shows that coupling alone raises the 30-year terrain-amplified failure probability from 14.8% to 24.1%, confirming that neglecting interaction effects is non-conservative.

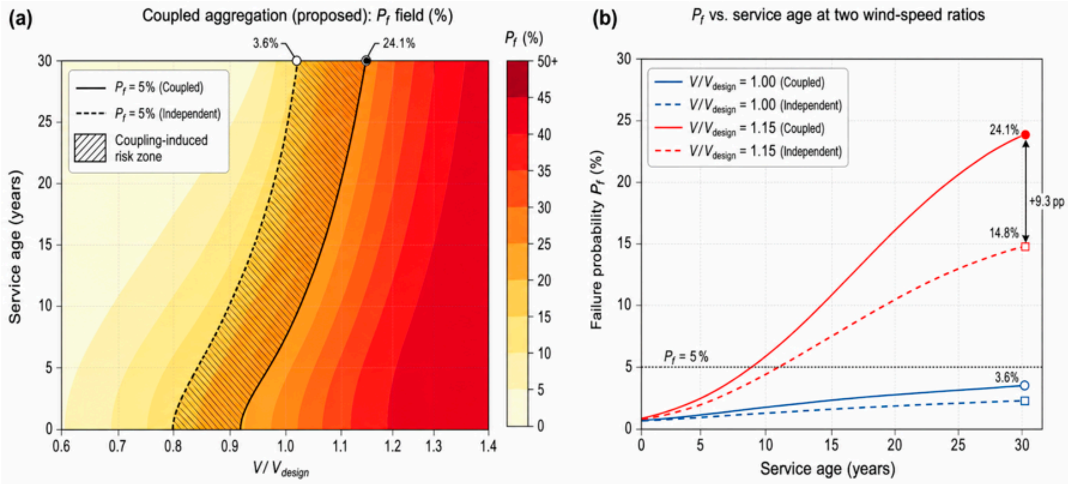

Figure 8. Failure probability P_f versus wind-speed ratio (V/V_design) and service age under two assumptions: four-factor coupled aggregation (proposed) and independent superposition. (**a**) Full-field map of the coupled P_f; solid and dashed lines are the P_f = 5% boundaries for the coupled and independent cases, and the hatched band between them is the coupling-induced risk zone. Open and filled circles mark the 30-year values under code wind (P_f = 3.6%) and terrain-amplified wind (P_f = 24.1%). (**b**) P_f versus service age at the two wind levels (cool: code; warm: terrain), solid = coupled, dashed = independent; at 30 years under terrain wind, coupling raises P_f from 14.8% to 24.1% (+9.3 pp). Dotted line: P_f = 5%.

Figure 9 displays the four-tier risk map of the tower at three service ages (10, 20, and 30 years) under the terrain-amplified wind scenario. At 10 years, 87% of members are Level I (safe), 11% are Level II (attention), and 2% are Level III (warning). By 20 years, the proportions shift to 62% Level I, 24% Level II, 12% Level III, and 2% Level IV (critical). At 30 years, 38% of members are Level I, 30% Level II, 21% Level III, and 11% Level IV, with the critical members concentrated in the base zone and hip connections.

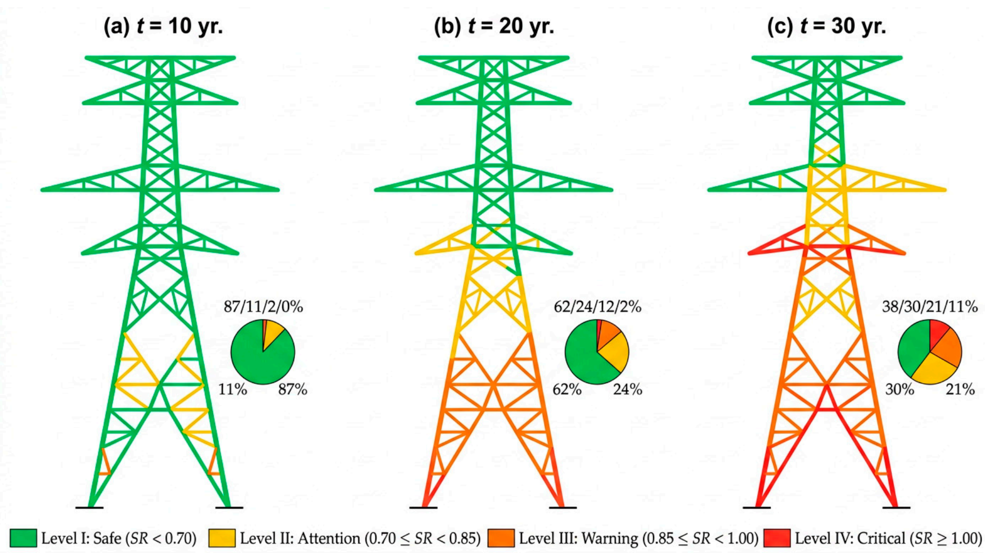

Figure 9. Four-tier risk map of the tower at service ages of (**a**) 10, (**b**) 20, and (**c**) 30 years under terrain-amplified wind (Scenario C). Colors: green = Level I (Safe), yellow = Level II (Attention), orange = Level III (Warning), red = Level IV (Critical).

A targeted reinforcement strategy is evaluated for the 30-year state: the five highest-priority members (three base-zone main legs and two hip-section connection members) are reinforced by replacing their sections with the next larger standard angle-steel profile. Figure 10 compares the member-level load-carrying capacity before and after reinforcement. The reinforcement increases the total tower steel mass by only 168 kg (2.8% of the total 6020 kg), yet it restores the tower-level SHI from 0.76 to 1.25 under the terrain-amplified wind, effectively extending the safe service life by at least an additional decade. The failure probability drops from 24.1% (17–33%) to 2.1% (1.2–3.6%), bringing the tower back within conventional reliability targets [31,35].

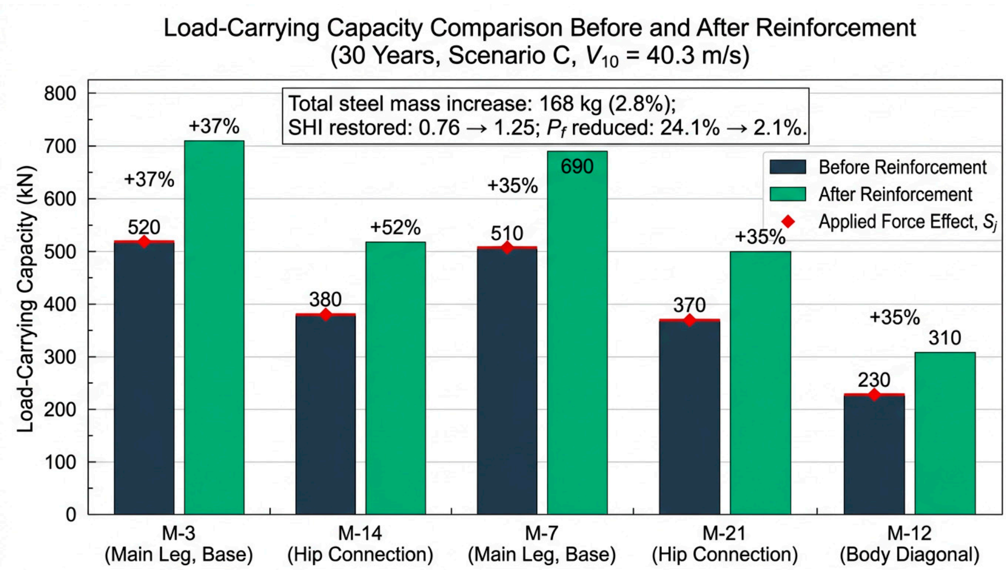

Figure 10. Comparison of member-level load-carrying capacity before and after reinforcement for the five most critical members at 30 years. Dark bars: before reinforcement; light bars: after reinforcement.

4.6. Impact of Terrain-Induced Wind Amplification on Safety Assessment

The results clearly demonstrate that terrain-induced wind amplification is a first-order factor in the safety assessment of transmission towers in mountainous coastal areas. At the case-study site, a moderate ridge with a slope of 22° produces a 15% speed-up at 10 m height [4,13], which translates into a 32% increase in wind load. This amplification alone is sufficient to reduce the intact tower's SHI from 1.47 to 1.11—still safe, but with more than half of the design reserve consumed. For the 30-year aged tower, the same terrain amplification shifts the SHI from 1.00 (borderline safe under code wind) to 0.76 (clearly unsafe), corresponding to a failure probability increase from 3.6% to 24.1%. These findings corroborate the field observations reported in the transmission line failure investigation literature [11,47], which frequently identify "wind speed exceeding the design basis due to topographic effects" as a primary or contributing cause of tower collapse. The implication for practice is unequivocal: for towers sited on or near terrain features that are known to amplify wind (ridges, escarpments, saddle points, valley mouths), a site-specific wind assessment—rather than the blanket code value—should be a prerequisite for safety evaluation [14,15].

4.7. Significance of Multi-Degradation Coupling

The comparison among single-factor, four-factor independent, and four-factor coupled assessment strategies (Section 4.3) provides quantitative evidence that degradation coupling is not merely a theoretical concern but a practically significant effect. At 30 years in a C4 environment, the coupled assessment yields a 32% total capacity loss for the critical member, versus 19.6% from corrosion-only and 25.0% from independent four-factor analysis. While the absolute magnitude of the coupling-induced "extra" loss (7 percentage points beyond independent superposition) may appear modest in isolation, its impact on the safety margin is decisive: it is the difference between SHI = 1.10 (still safe) and SHI = 1.00 (at the failure boundary). Perhaps more importantly, coupling alters the weak-component ranking (Figure 7), promoting connection-zone members to the top of the vulnerability list. An operator who relies on corrosion-rate measurements alone would correctly identify the base zone as the most corroded region but would miss the elevating risk at bolt connections in the waist section—precisely the kind of "hidden" vulnerability that the coupled assessment is designed to reveal. This finding aligns with the broader structural reliability literature [19,20,30] on time-dependent multi-hazard analysis, which consistently shows that interaction effects can shift the dominant failure mode and invalidate single-factor inspection strategies.

The dominance of the corrosion–fatigue pathway in Figure 5 is mechanistically rooted in the cubic form of the S–N law: a section-loss fraction η_c inflates the stress range by $1/(1-\eta_c)$, and because cycles-to-failure scale with $(\Delta\sigma)^{-3}$, even a 15–20% area loss roughly doubles the local fatigue-damage rate. Physically, the decelerating corrosion exponent $n = 0.59$ reflects the build-up of a partially protective oxide/rust film (predominantly goethite–lepidocrocite for low-alloy steel in chloride atmospheres) that throttles oxygen and chloride diffusion; where this film is mechanically disrupted by fretting at bolted laps or spalled by wet–dry cycling, the local rate can transiently revert toward linear growth, accelerating both section loss and pit initiation. It must be stated explicitly as a limitation that the present coupling matrix is derived from analytical/empirical laws and is not corroborated by post-mortem metallography or oxide-film characterization of service-exposed members; the matrix should, therefore, be regarded as a screening-level quantification, and experimental validation (cross-sectional micrographs, pit-depth statistics, and rust-layer phase analysis for each mechanism) is identified as a priority for future work.

4.8. Comparison with Current Code-Based Practice

Current international standards for transmission tower structural design (IEC 60826 [1], EN 50341 [2], ASCE 74 [3]) prescribe a single-point verification against factored design loads, implicitly assuming that the structure retains its as-designed capacity throughout its service life. The reliability index embedded in these standards (typically β = 2.0–2.5 for ultimate limit states [1,31]) is calibrated for the intact condition and does not account for progressive degradation. The RBSAF framework proposed in this paper is not intended to replace these design standards but to complement them with a time-variant assessment capability that is essential for in-service safety management. Specifically, the code verification answers the question "Is the new tower safe against the design basis event?", while the RBSAF answers the more operationally relevant question "How much safety margin does this aging tower still possess, and where is it most likely to fail?" The two approaches are entirely consistent: the RBSAF uses the same material strengths, load formulations, and stability criteria as the applicable codes, but applies them to a progressively degraded structural state and a terrain-refined wind input [33,41]. Future revisions of design standards may benefit from incorporating provisions for periodic reassessment with degradation modeling, a practice already established in the bridge engineering community [18,19].

4.9. Computational Efficiency and Engineering Practicality

The RBSAF framework has been implemented in a Python-based computational platform and tested on a standard workstation (Intel Core i7, 32 GB RAM). The wind simulation module requires approximately 2 min per inflow direction for the 5 km × 5 km domain at 10 m resolution. The structural finite element solution takes less than 0.5 s per load case. The degradation computation, coupling aggregation, and SR calculation are algebraic operations that execute in negligible time. A complete assessment of one tower across all four service ages, 24 wind directions, and 9 wind speed levels (=864 scenarios) is completed in approximately 50 min of wall-clock time, including wind simulation. This throughput is sufficient for batch-processing a transmission line corridor of several hundred towers within a few days on a multi-core workstation—a dramatic improvement over the weeks or months that a traditional CFD-based approach would require [14,15,46]. The framework's modular architecture also supports easy parallelization: the wind simulations for different tower sites can be distributed across multiple cores or cloud instances with near-linear scalability.

4.10. Limitations and Future Work

Several limitations of the present study should be acknowledged. First, the degradation model parameters (corrosion coefficients, bolt loosening rate, S–N detail category, pitting dimensions) are derived from the open literature and standard specifications, not from site-specific inspection data. While these values are representative of the C4 corrosion class, actual degradation rates can vary depending on local microclimate, coating condition, and maintenance history. A variance-based global sensitivity analysis (first-order Sobol' indices) has been incorporated to rank the significance of the degradation mechanisms (Section 4.3); its extension to total-order indices and to spatially distributed parameter fields remains for future work. Calibration with field inspection data (e.g., in-situ ultrasonic thickness measurements, bolt torque audits, and metallographic pit-depth surveys) would further sharpen the assessment for a specific tower and is the recommended path for engineering deployment. Second, the structural model assumes axial-force-only members (truss idealization), which cannot capture secondary bending effects at eccentrically loaded connections. A beam-element model with semi-rigid connections would provide a more accurate representation of the load redistribution under bolt loosening, at the cost of increased computational effort. Third, additional degradation mechanisms not addressed in this study—such as foundation deterioration, conductor icing, and environmental stress corrosion cracking—may contribute to capacity loss in certain climatic regions and should be incorporated in future extensions. In addition, the corrosion model treats each zone as undergoing uniform general corrosion and does not resolve (i) macro-galvanic coupling between the dissimilar materials in the assembly—Q345 and Q235 members, Grade 8.8 fasteners, and the zinc coating—which can locally accelerate anodic dissolution, nor (ii) crevice and autocatalytic pitting cells that develop within bolted lap joints and faying surfaces, where occluded acidification and chloride enrichment sustain localized attack. These electrochemically driven, location-specific mechanisms would tend to concentrate damage at connections beyond the uniform-zone estimate adopted here; their explicit treatment, together with the protective effect and eventual depletion of the hot-dip-galvanized layer, is an important refinement for future versions of the framework. Fourth, the failure probability estimates are based on deterministic degradation models with a single set of parameters; a full probabilistic treatment using Monte Carlo simulation with parameter distributions would provide more robust reliability estimates [32,34,36]. Finally, dynamic wind effects (buffeting, aeroelastic interactions) are not explicitly modeled; the quasi-static approach adopted here is consistent with current design practice [1,3,48] but may underestimate the peak response in highly turbulent terrain. Addressing these limitations constitutes the natural next steps of this research program. Finally, dynamic wind effects (buffeting, resonant amplification, aeroelastic interactions) are not explicitly modeled. The quasi-static approach adopted here uses the gust (peak) wind speed and, therefore, already captures the quasi-static (background) turbulence response, consistent with current design practice [1,3,48]; what it omits is the resonant contribution at the tower's fundamental frequency. The magnitude of this omission was estimated a posteriori for the case-study tower using the Davenport gust-factor decomposition [12], with f_1 = 2.4 Hz, a structural damping ratio of 1%, and the site turbulence intensity. Because f_1 = 2.4 Hz lies well into the high-frequency, low-energy tail of the wind spectrum, the resonant component is small—it adds an estimated 8–12% to the peak member forces and base shear. This amplification is modest for the present stiff tower but would grow for more flexible structures (lower f_1) and is more consequential for fatigue, where the resonant peak contributes disproportionately to the stress-cycle spectrum; the fatigue damage of vibration-prone waist diagonals and of loosened bolted connections may, therefore, be underestimated by a larger relative margin. A full buffeting/aeroelastic treatment, which would also refine the bolt-loosening cycle count of Section 2.3.2, is identified as a priority extension.

5. Conclusions

This paper proposed a Risk-Based Safety Assessment Framework (RBSAF) for aging lattice steel space-truss structures under extreme wind, integrating terrain-resolved wind simulation with multi-degradation coupling, and demonstrated it on a 220 kV angle-steel tower. The principal findings are:

(1). Terrain amplification is a first-order load effect. A 15% ridge-top speed-up raises the wind load by ~32% and lowers the intact SHI from 1.47 to 1.11 and the 30-year coupled SHI from 1.00 to 0.76 (failure probability 3.6% → 24.1%)—a deficit invisible to uniform code wind.

(2). Multi-degradation coupling is decisive, not marginal. Corrosion–fatigue synergy dominates; the coupled assessment gives 32% capacity loss for the critical member (28% more than corrosion-only, 9.3% more than independent four-factor superposition) and reorders the weak-component ranking to promote bolted-connection members that single-factor inspection would miss.

(3). A unified, time-variant Structural Health Index (SHI) combining four coupled mechanisms with terrain-resolved wind provides a single, code-consistent metric for tracking residual safety margin across service age, wind speed, and direction.

(4). Risk-informed reinforcement is highly cost-effective. Replacing five critical members (+2.8% steel mass) restores the SHI from 0.76 to 1.25 and cuts the failure probability from 24.1% to 2.1%, extending the safe service life by at least a decade.

These conclusions are subject to the parameter and modeling uncertainties quantified above; site-specific inspection calibration, explicit electrochemical (galvanic/crevice) corrosion mechanisms, full probabilistic Monte-Carlo treatment, and experimental metallographic validation are the priority next steps. Although demonstrated on a transmission tower, the RBSAF architecture—the five-step pipeline of hazard characterization, vulnerability modeling, coupling aggregation, margin scanning, and risk ranking—is generic, and its hazard and structural modules are deliberately interface-based and hence, reusable without modification. Transfer to other lattice systems is, therefore, a matter of module recalibration rather than architectural redesign for structures that share the same dominant physics (communication and observation towers, lattice roofs, industrial space frames). For systems governed by different mechanisms—weld fatigue and stress-corrosion cracking in welded or tubular supports, bearing wear in rotating-equipment masts—or by different aerodynamic regimes (galloping, vortex-induced vibration), the

https://doi.org/10.3390/app16136788

degradation and load modules must be extended with the corresponding sub-models, while the coupling, scanning, and risk-ranking layers remain unchanged. The framework is thus best described as a universal architecture with application-specific degradation and load modules, rather than a turnkey solution for every lattice typology.

Author Contributions: Conceptualization, Y.W. and D.H.; methodology, Y.W., H.Z., and D.H.; software, H.Z. and J.C.; validation, D.Y., H.Z., and J.C.; formal analysis, Y.W. and H.Z.; investigation, Y.W. and D.Y.; resources, D.Y.; data curation, J.C.; writing—original draft preparation, Y.W. and H.Z.; writing—review and editing, D.H.; visualization, H.Z. and J.C.; supervision, D.H.; project administration, D.Y.; funding acquisition, D.Y. and D.H. All authors have read and agreed to the published version of the manuscript.

Funding: This research received no external funding.

Institutional Review Board Statement: Not applicable.

Informed Consent Statement: Not applicable.

Data Availability Statement: The data presented in this study are available on request from the corresponding author. The data are not publicly available due to confidentiality requirements of the partner utility company.

Conflicts of Interest: Authors Yu Wang and Dedong Yang are employed by State Grid Wenzhou Electric Power Supply Company. The remaining authors declare that the research was conducted in the absence of any commercial or financial relationships that could be construed as a potential conflict of interest. The funders had no role in the design of the study; in the collection, analyses, or interpretation of data; in the writing of the manuscript; or in the decision to publish the results.

References

1. *IEC 60826:2017*; Design Criteria of Overhead Transmission Lines. International Electrotechnical Commission (IEC): Geneva, Switzerland, 2017.
2. *EN 50341-1:2012*; Overhead Electrical Lines Exceeding AC 1 kV—Part 1: General Requirements—Common Specifications. European Committee for Electrotechnical Standardization (CENELEC): Brussels, Belgium, 2012.
3. ASCE. *Guidelines for Electrical Transmission Line Structural Loading*, 4th ed.; ASCE Manuals and Reports on Engineering Practice No. 74; American Society of Civil Engineers: Reston, VA, USA, 2020.
4. Holmes, J.D. *Wind Loading of Structures*, 3rd ed.; CRC Press: Boca Raton, FL, USA, 2015.
5. Simiu, E.; Yeo, D.H. *Wind Effects on Structures: Modern Structural Design for Wind*, 4th ed.; John Wiley & Sons: Hoboken, NJ, USA, 2019.
6. CIGRÉ. *Current Practices Regarding Frequencies and Magnitude of High Intensity Winds*; Technical Brochure No. 256; CIGRÉ Working Group B2.16: Paris, France, 2004.
7. Panteli, M.; Mancarella, P. Influence of Extreme Weather and Climate Change on the Resilience of Power Systems: Impacts and Possible Mitigation Strategies. *Electr. Power Syst. Res.* **2015**, *127*, 259–270. https://doi.org/10.1016/j.epsr.2015.06.012.
8. Bruneau, M.; Chang, S.E.; Eguchi, R.T.; Lee, G.C.; O'Rourke, T.D.; Reinhorn, A.M.; Shinozuka, M.; Tierney, K.; Wallace, W.A.; von Winterfeldt, D. A Framework to Quantitatively Assess and Enhance the Seismic Resilience of Communities. *Earthq. Spectra* **2003**, *19*, 733–752. https://doi.org/10.1193/1.1623497.
9. Ouyang, M. Review on Modeling and Simulation of Interdependent Critical Infrastructure Systems. *Reliab. Eng. Syst. Saf.* **2014**, *121*, 43–60. https://doi.org/10.1016/j.ress.2013.06.040.
10. Tian, L.; Ma, R.; Li, H.; Wang, Y. Progressive Collapse of Power Transmission Tower-Line System Under Extremely Strong Earthquake Excitations. *Int. J. Struct. Stab. Dyn.* **2016**, *16*, 1550030. https://doi.org/10.1142/S0219455415500303.
11. Rao, N.P.; Knight, G.M.S.; Lakshmanan, N.; Iyer, N.R. Investigation of Transmission Line Tower Failures. *Eng. Fail. Anal.* **2010**, *17*, 1127–1141. https://doi.org/10.1016/j.engfailanal.2010.01.008.
12. Davenport, A.G. The Application of Statistical Concepts to the Wind Loading of Structures. *Proc. Inst. Civ. Eng.* **1961**, *19*, 449–472. https://doi.org/10.1680/iicep.1961.11304.

13. Jackson, P.S.; Hunt, J.C.R. Turbulent Wind Flow over a Low Hill. *Q. J. R. Meteorol. Soc.* **1975**, *101*, 929–955. https://doi.org/10.1002/qj.49710143015.
14. Bitsuamlak, G.T.; Stathopoulos, T.; Bédard, C. Numerical Evaluation of Wind Flow over Complex Terrain: Review. *J. Aerosp. Eng.* **2004**, *17*, 135–145. https://doi.org/10.1061/(ASCE)0893-1321(2004)17:4(135).
15. Uchida, T.; Ohya, Y. Large-Eddy Simulation of Turbulent Airflow over Complex Terrain. *J. Wind Eng. Ind. Aerodyn.* **2003**, *91*, 219–229. https://doi.org/10.1016/S0167-6105(02)00347-1.
16. Raissi, M.; Perdikaris, P.; Karniadakis, G.E. Physics-Informed Neural Networks: A Deep Learning Framework for Solving Forward and Inverse Problems Involving Nonlinear Partial Differential Equations. *J. Comput. Phys.* **2019**, *378*, 686–707. https://doi.org/10.1016/j.jcp.2018.10.045.
17. Kashinath, K.; Mustafa, M.; Albert, A.; Wu, J.-L.; Jiang, C.; Esmaeilzadeh, S.; Azizzadenesheli, K.; Wang, R.; Chattopadhyay, A.; Singh, A.; et al. Physics-Informed Machine Learning: Case Studies for Weather and Climate Modelling. *Phil. Trans. R. Soc. A* **2021**, *379*, 20200093. https://doi.org/10.1098/rsta.2020.0093.
18. Kayser, J.R.; Nowak, A.S. Reliability of Corroded Steel Girder Bridges. *Struct. Saf.* **1989**, *6*, 53–63. https://doi.org/10.1016/0167-4730(89)90007-6.
19. Stewart, M.G.; Rosowsky, D.V. Time-Dependent Reliability of Deteriorating Reinforced Concrete Bridge Decks. *Struct. Saf.* **1998**, *20*, 91–109. https://doi.org/10.1016/S0167-4730(97)00021-0.
20. Ghosh, J.; Padgett, J.E. Aging Considerations in the Development of Time-Dependent Seismic Fragility Curves. *J. Struct. Eng.* **2010**, *136*, 1497–1511. https://doi.org/10.1061/(ASCE)ST.1943-541X.0000260.
21. *ISO 9223:2012*; Corrosion of Metals and Alloys—Corrosivity of Atmospheres—Classification, Determination and Estimation. International Organization for Standardization (ISO): Geneva, Switzerland, 2012.
22. Landolfo, R.; Cascini, L.; Portioli, F. Modeling of Metal Structure Corrosion Damage: A State of the Art Report. *Sustainability* **2010**, *2*, 2163–2175. https://doi.org/10.3390/su2072163.
23. Rahgozar, R. Remaining Capacity Assessment of Corrosion Damaged Beams Using Minimum Curves. *J. Constr. Steel Res.* **2009**, *65*, 299–307. https://doi.org/10.1016/j.jcsr.2008.02.004.
24. Junker, G.H. New Criteria for Self-Loosening of Fasteners Under Vibration. *SAE Trans.* **1969**, *78*, 314–335. https://doi.org/10.4271/690055.
25. Bickford, J.H. *Introduction to the Design and Behavior of Bolted Joints: Non-Gasketed Joints*, 4th ed.; CRC Press: Boca Raton, FL, USA, 2007.
26. Huda, F.; Kajiwara, I.; Hosoya, N.; Kawamura, S. Bolt Loosening Analysis and Diagnosis by Non-Contact Laser Excitation Vibration Tests. *Mech. Syst. Signal Process.* **2013**, *40*, 589–604. https://doi.org/10.1016/j.ymssp.2013.05.023.
27. *EN 1993-1-9:2005*; Eurocode 3: Design of Steel Structures—Part 1-9: Fatigue. European Committee for Standardization (CEN): Brussels, Belgium, 2005.
28. Miner, M.A. Cumulative Damage in Fatigue. *J. Appl. Mech.* **1945**, *12*, A159–A164. https://doi.org/10.1115/1.4009458.
29. Cerit, M.; Genel, K.; Eksi, S. Numerical Investigation on Stress Concentration of Corrosion Pit. *Eng. Fail. Anal.* **2009**, *16*, 2467–2472. https://doi.org/10.1016/j.engfailanal.2009.04.004.
30. Melchers, R.E.; Beck, A.T. *Structural Reliability Analysis and Prediction*, 3rd ed.; John Wiley & Sons: Hoboken, NJ, USA, 2018.
31. Ellingwood, B.R. Probability-Based Codified Design: Past Accomplishments and Future Challenges. *Struct. Saf.* **1994**, *13*, 159–176. https://doi.org/10.1016/0167-4730(94)90024-8.
32. Ditlevsen, O.; Madsen, H.O. *Structural Reliability Methods*; John Wiley & Sons: Chichester, UK, 1996.
33. Nowak, A.S.; Collins, K.R. *Reliability of Structures*, 2nd ed.; CRC Press: Boca Raton, FL, USA, 2012.
34. Thoft-Christensen, P.; Baker, M.J. *Structural Reliability Theory and Its Applications*; Springer: Berlin/Heidelberg, Germany, 1982.
35. Cornell, C.A. A Probability-Based Structural Code. *ACI J.* **1969**, *66*, 974–985. https://doi.org/10.14359/7446.
36. Ang, A.H.-S.; Tang, W.H. *Probability Concepts in Engineering: Emphasis on Applications to Civil and Environmental Engineering*, 2nd ed.; John Wiley & Sons: Hoboken, NJ, USA, 2007.
37. Cai, Y.; Xie, Q.; Xue, S.; Hu, L.; Kareem, A. Fragility Modelling Framework for Transmission Line Towers Under Winds. *Eng. Struct.* **2019**, *191*, 686–697. https://doi.org/10.1016/j.engstruct.2019.04.096.
38. Shinozuka, M.; Feng, M.Q.; Lee, J.; Naganuma, T. Statistical Analysis of Fragility Curves. *J. Eng. Mech.* **2000**, *126*, 1224–1231. https://doi.org/10.1061/(ASCE)0733-9399(2000)126:12(1224).
39. *EN 1991-1-4:2005*; Eurocode 1: Actions on Structures—Part 1–4: General Actions—Wind Actions. European Committee for Standardization (CEN): Brussels, Belgium, 2005.

40. Mara, T.G.; Hong, H.P. Effect of Wind Direction on the Response and Capacity Surface of a Transmission Tower. *Eng. Struct.* **2013**, *57*, 493–501. https://doi.org/10.1016/j.engstruct.2013.10.004.
41. *EN 1993-1-1:2005*; Eurocode 3: Design of Steel Structures—Part 1-1: General Rules and Rules for Buildings. European Committee for Standardization (CEN): Brussels, Belgium, 2005.
42. Melchers, R.E. Pitting Corrosion of Mild Steel in Marine Immersion Environment—Part 1: Maximum Pit Depth. *Corrosion* **2004**, *60*, 824–836.
43. Jin, L.; Zhang, X.; Liang, X.; Wang, Z.; Wu, Q. Mechanical properties of corroded carbon steel based on random pit corrosion in marine environment. *Ocean Eng.* **2022**, *260*, 111759.
44. Lin, B.; Hu, R.; Ye, C.; Li, Y.; Lin, C. A Study on the Initiation of Pitting Corrosion in Carbon Steel in Chloride-Containing Media Using Scanning Electrochemical Probes. *Electrochim. Acta* **2010**, *55*, 6542–6545.
45. Albermani, F.; Kitipornchai, S. Numerical Simulation of Structural Behaviour of Transmission Towers. *Thin-Walled Struct.* **2003**, *41*, 167–177. https://doi.org/10.1016/S0263-8231(02)00085-X.
46. Lee, P.-S.; McClure, G. Elastoplastic Large Deformation Analysis of a Lattice Steel Tower Structure and Comparison with Full-Scale Tests. *J. Constr. Steel Res.* **2007**, *63*, 709–717. https://doi.org/10.1016/j.jcsr.2006.06.041.
47. Savory, E.; Parke, G.A.R.; Zeinoddini, M.; Toy, N.; Disney, P. Modelling of Tornado and Microburst-Induced Wind Loading and Failure of a Lattice Transmission Tower. *Eng. Struct.* **2001**, *23*, 365–375. https://doi.org/10.1016/S0141-0296(00)00045-6.
48. Fu, X.; Li, H.-N. Dynamic Analysis of Transmission Tower-Line System Subjected to Wind and Rain Loads. *J. Wind Eng. Ind. Aerodyn.* **2016**, *157*, 95–103. https://doi.org/10.1016/j.jweia.2016.08.010.